Twin-S: A Digital Twin for Skull-base Surgery

Hongchao Shu[1*†], Ruixing Liang[1,2†], Zhaoshuo Li[1†], Anna Goodridge[1], Xiangyu Zhang[1], Hao Ding[1], Nimesh Nagururu[2], Manish Sahu[1], Francis X. Creighton[2], Russell H. Taylor[1], Adnan Munawar[1] and Mathias Unberath[1]

[1]Johns Hopkins University, Baltimore, MD, United States.
[2]Johns Hopkins Medicine, Baltimore, MD, United States.

*Corresponding author(s). E-mail(s): hshu4@jhu.edu;
†These authors are joint first authors.

Abstract

Purpose: Digital twins are virtual interactive models of the real world, exhibiting identical behavior and properties. In surgical applications, computational analysis from digital twins can be used, for example, to enhance situational awareness. **Methods:** We present a digital twin framework for skull-base surgeries, named Twin-S, which can be integrated within various image-guided interventions seamlessly. Twin-S combines high-precision optical tracking and real-time simulation. We rely on rigorous calibration routines to ensure that the digital twin representation precisely mimics all real-world processes. Twin-S models and tracks the critical components of skull-base surgery, including the surgical tool, patient anatomy, and surgical camera. Significantly, Twin-S updates and reflects real-world drilling of the anatomical model in frame rate. **Results:** We extensively evaluate the accuracy of Twin-S, which achieves an average 1.39 mm error during the drilling process. We further illustrate how segmentation masks derived from the continuously updated digital twin can augment the surgical microscope view in a mixed reality setting, where bone requiring ablation is highlighted to provide surgeons additional situational awareness. **Conclusion:** We present Twin-S, a digital twin environment for skull-base surgery. Twin-S tracks and updates the virtual model in real-time given measurements from modern tracking technologies.

Future research on complementing optical tracking with higher-precision vision-based approaches may further increase the accuracy of Twin-S.

Keywords: Image-guided Intervention; Computer Vision; Human-computer Interaction; Intervention Planning and Simulation

1 Introduction

Digital twins are virtual counterparts of real-world processes, modeling real-world dynamics and properties in real-time [1]. Receiving continuous measurements from sensor-rich environments, digital twins can conversely provide computational feedback to the real entity. Digital twins have shown great benefits in areas of manufacturing, farming, and product design [2].

In surgical scenarios, digital twins have the potential to offer advantages across all surgical stages (Figure 1). Prior work has explored the use of digital twins in pre-operative planning and immersive training [3]. When used intra-operatively, digital twins can further provide real-time guidance to surgeons for complementary situational awareness and, in turn, facilitate surgical decision-making [4–6]. Such feedback from a digital twin can be crucial when direct observations in the operating room are heterogeneous and complex. For instance, poor visibility of the target anatomy due to blood and occlusion by surgical tools can be supplemented with information from the digital twins to provide the surgeon with enhanced situational awareness. Lastly, digital twins can fully digitize surgical procedures for record-keeping, comprehensive post-operative evaluation, surgical training, and dataset generation for machine learning algorithm development.

Augmented Reality (AR) and Virtual Reality (VR) are closely related to digital twins systems and have been widely adopted for surgical applications [7]. Most prior AR systems overlay the pre-operative scans or plans on the patient anatomy for intra-operative guidance [8]. However, these systems do not update the patient model intra-operatively, limiting the utility of these systems in surgical practice [9]. VR systems, on the other hand, mainly focus on simulations for surgical training [10]. These VR systems do not receive measurements from the real world, thus fail to mimic the behaviors of the physical entities in real-time [11]. Concurrent to our work, Shi *et al.* [12] use the digital twins paradigm in liver tumor surgery. A virtual model is used to predict the motion of the liver for respiratory compensation. Several other works have used the digital twins framework to realize telesurgery [13, 14]. To reduce the bandwidth requirement of network communication, they proposed to replace the visualization of remote scenes entirely with renderings of local simulation. Thus, only poses of objects are required to be communicated through the network. However, they did not quantitatively evaluate the matching between digital twin and physical entity, reducing the fidelity of the twins.

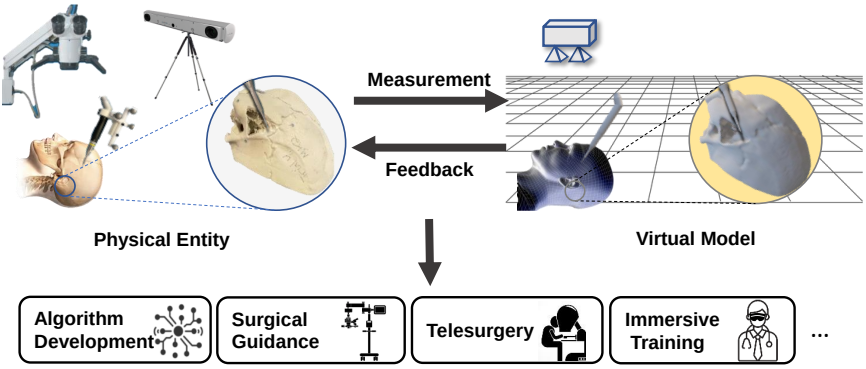

Fig. 1 Overview of our Twin-S digital twin concept and associated applications. Measurements are collected from various sensors deployed in the operating room and sent to the virtual model continuously. The feedback from the computation analysis of the virtual model is provided to the physical entity, which can be used in many downstream applications.

We present a digital twins framework for skull-base surgeries, named Twin-S, which can seamlessly integrate within various image-guided interventions. We specifically consider mastoidectomy [15], a surgical approach in the lateral skull base whereby bone is removed with surgical drills to obtain access to the middle and inner ear. Given the complex arrangement of cortical bone, nerves, vasculature and end-organs, surgical stereo microscopes are used to navigate in the small operating field. Twin-S combines high-precision optical tracking and real-time simulation to create digital twins for skull-base surgery. We rely on rigorous calibration routines to ensure that the digital twin representation precisely mimics all real-world processes. Twin-S models and tracks the critical components of skull-base surgery, including the surgical tool, patient anatomy, and surgical camera. Significantly, Twin-S updates patient anatomy to account for the real-world tool to tissue interactions at a frame rate of 28 FPS.

To evaluate the effectiveness of Twin-S, we conduct thorough experiments assessing the accuracy of Twin-S. We further derive numerical analysis to provide maximum bounds on tracking error and the contribution to the final error from different components. Finally, we illustrate one use case of Twin-S in a mixed-reality setup. The segmentation masks of pre-planned targets are generated and overlaid on the surgical field. Tissue encasing these deeper seated targets and requiring removal is highlighted and color-coded as real-time visual assistance, which provides complementary situational awareness to the users.

The contributions of our work can be summarized as follows:

- We present a digital twin framework for skull base surgery named Twin-S. It models, tracks and updates all critical components of skull-base surgeries in real-time.

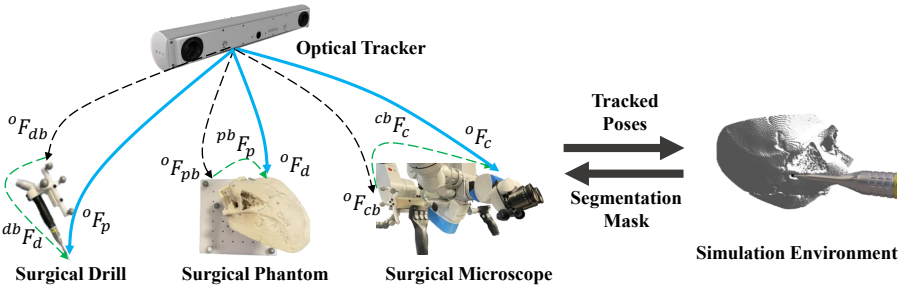

Fig. 2 Overview of the physical setup of Twin-S for skull-base surgery. Twin-S models, tracks, and updates the surgical drill $^{o}\mathrm{F}_{d}$, the surgical phantom $^{o}\mathrm{F}_{p}$, and surgical camera $^{o}\mathrm{F}_{c}$ to emulate the clinical setting.

- We present numerical analysis of tracking error to shed insights on the worst case error bounds and error sources. We further showcase one application of Twin-S in downstream tasks such as mixed reality.

2 System Components

Building a digital twin system for skull-base surgery requires precise modeling, tracking, and updating of the patient's anatomy, the surgeon's tool(s), and the surgical camera. In our setup, the system includes a surgical phantom to simulate the patient's anatomy, a surgical drill as the ablation tool, and a stereo surgical microscope. Twin-S acquires 3D poses of each component via an optical tracker (FusionTrack 500, Atracsys). The pose measurements are streamed into a physics-based real-time virtual environment built upon AMBF [11]. The virtual environment provides computational analysis as feedback to the real-world processes. For example, Twin-S generates per-pixel segmentation information of the surgical scene for downstream tasks. The three poses of interest are the $\mathbb{SE}(3)$ transformations from the optical tracker to the camera $^{o}\mathrm{F}_{c}$, the surgical drill $^{o}\mathrm{F}_{d}$ and the surgical phantom $^{o}\mathrm{F}_{p}$. An overview of our physical setup is shown in Figure 2.

2.1 Modeling of the Surgical Drill

The 3D model of the surgical tool is obtained from its manufacturer (ANSPACH, Johnson & Johnson). In Twin-S, we assign the drill coordinate frame to the drill tip center. We mount 4 optical tracking markers at the tail of the drill shaft, defining the base frame of the drill. The pose of surgical tool $^{o}\mathrm{F}_{d}$ is thus defined as:

$$^{o}\mathrm{F}_{d} = {}^{o}\mathrm{F}_{db} \cdot {}^{db}\mathrm{F}_{d}, \text{ where } {}^{db}\mathrm{F}_{d} = \begin{bmatrix} {}^{db}\mathrm{R}_{d} & {}^{db}\mathrm{t}_{d} \\ 0 & 1 \end{bmatrix}. \tag{1}$$

where the transformation of the drill base in the optical tracker coordinate $^{o}\mathrm{F}_{db}$ is measured directly. Calibrations are required for both the rotational and

the translational components of ${}^{db}\mathrm{F}_d$, which transforms the base coordinate at the tail to the drill coordinate at the drill tip.

The translational component ${}^{db}\mathrm{t}_d$ is obtained by pivot calibration [16]. For the rotational component ${}^{db}\mathrm{R}_d$, it is only necessary to calibrate the direction of the drill shaft axis w.r.t the optical tracker coordinate system as the drill is symmetrical along its shaft. We fix the drill on a robot arm end effector and command the robot to move along the drill shaft axis. Hence, the calibration problem reduces to recovering the rotation between two linear trajectories, the trajectory defined in the drill shaft axis P and the optical tracked trajectory Q. We use Kabsch algorithm [17] to recover the optimal solution for ${}^{db}\mathrm{R}_d$ via least squares:

$$ {}^{db}\mathrm{R}_d = (H^T H)^{\frac{1}{2}} H^{-1}, \text{ where } H = P^T Q. \tag{2} $$

2.2 Modeling of the Surgical Phantom

We obtain the 3D structure of the surgical phantom using a CT scanner. The phantom is modeled as a binary volume of occupancy, where voxels corresponding to the bony tissues are marked as occupied and voxels representing air are marked as free space. To track the surgical phantom, we rigidly mount the phantom on a polycarbonate board with 5 optical tracking markers, defining the base coordinate of the phantom. The pose of the phantom ${}^{o}\mathrm{F}_p$ is:

$$ {}^{o}\mathrm{F}_p = {}^{o}\mathrm{F}_{pb} \cdot {}^{pb}\mathrm{F}_p \,, \tag{3} $$

where the transformation of the phantom base in the optical tracker coordinate ${}^{o}\mathrm{F}_{pb}$ is measured directly. We describe our approach to calibrate the transformation from phantom base to phantom ${}^{pb}\mathrm{F}_p$ below.

To calibrate ${}^{pb}\mathrm{F}_p$, we directly compute the transformation between the virtual model and the physical phantom via the ICP algorithm [18]. We sample 380 points on the phantom surface using a tracked pointer tool, obtaining a point cloud defined in the tracker coordinate ${}^{o}P$. We also convert the binary volume to a set of point cloud, denoted as ${}^{m}P$. The transformation of the phantom in the phantom base coordinate ${}^{pb}\mathrm{F}_p$ can be easily computed by:

$$ {}^{pb}\mathrm{F}_p = \mathrm{ICP}({}^{o}P, {}^{m}P), \tag{4} $$

where we use the point-to-plane ICP registration between the sampled surface ${}^{o}P$ and the virtual model ${}^{m}P$.

2.3 Modeling Tool-to-tissue Interaction

When surgeons perform drilling in the real world, we update the surgical phantom in real-time. We approximate the drill tip as a sphere. Twin-S detects collisions between the surgical phantom and the drill burr given the tracked positions. The voxels that collide with the drill tip sphere are moved and set to

free space to simulate the tissue removal process. More details of the drilling algorithm can be found in [11].

2.4 Modeling of the Surgical Camera

We first obtain the intrinsic parameters and distortion coefficients of the stereo camera. We use Zhang's camera model [19] and calibrate the stereo camera using a ChArUco pattern. Rectification is then performed to obtain a projective camera model. To track the surgical camera, 4 optical tracking markers are mounted on the handle of the camera, defining the base coordinate frame. The pose of the camera is defined as:

$$ {}^{o}\mathrm{F}_{c} = {}^{o}\mathrm{F}_{cb} \cdot {}^{cb}\mathrm{F}_{c}\,, \tag{5} $$

where the transformation of the camera base w.r.t. the optical tracker ${}^{o}\mathrm{F}_{cb}$ is measured directly. A hand-eye calibration routine [20] is used to obtain ${}^{o}\mathrm{F}_{cb}$.

The hand-eye calibration is formulated as the $AX = XB$ problem, where $X = {}^{cb}\mathrm{F}_{c}$ (Figure 3). The camera is moved to different locations while a ChArUco calibration pattern is fixed in space. The transformation of the camera in the ChArUco pattern coordinate ${}^{u}\mathrm{F}_{c}$ is estimated. Given recorded poses ${}^{o}\mathrm{F}_{cb}$ and ${}^{u}\mathrm{F}_{c}$, for the t^{th} camera pose, we have:

$$ A_{[t]} \cdot {}^{cb}\mathrm{F}_{c} = {}^{cb}\mathrm{F}_{c} \cdot B_{[t]}, \tag{6} $$

where

$$ A_{[t]} = {}^{o}\mathrm{F}^{-1}_{cb_{[0]}} \cdot {}^{o}\mathrm{F}_{cb_{[t]}}, \quad B_{[t]} = {}^{c}\mathrm{F}_{u_{[0]}} \cdot {}^{c}\mathrm{F}^{-1}_{u_{[t]}} \tag{7} $$

are relative transformations between the optical tracked poses and ChArUco regressed poses.

We perform additional synchronization checks on the recorded poses and filter out outliers following the process described by Hutter *et al.* [21]. Given the tracked camera, Twin-S generates per-pixel segmentation based on the object information, which can be used for different downstream applications [11].

3 Experiments and Results

In the following sections, we conduct thorough experimental and numerical analysis on Twin-S to characterize its accuracy.

3.1 Optical Tracking Accuracy

We conduct experiments to evaluate the accuracy of the optical tracker, as its accuracy directly impacts the results of Twin-S. Throughout this experiment, we fix the location of the optical tracker. We start with mounting 4 optical markers on a 3-axis micrometer stage (Figure 4 (a)). For each experiment trial, we individually move 5 mm along the x, y, and z axis in the micrometer stage local coordinate. We conduct 3 trials in total, each with a new orientation w.r.t.

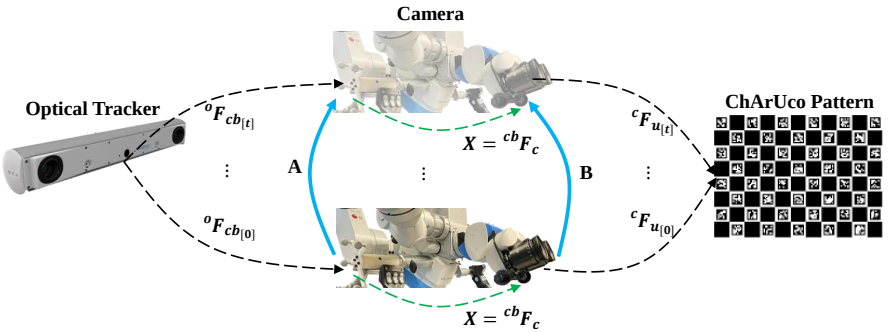

Fig. 3 Overview of the hand-eye calibration setup. The camera is moved to different locations. The relative transformation between optical tracker poses A and between ChArUco pattern poses B are computed for $X = {}^{cb}\mathrm{F}_c$.

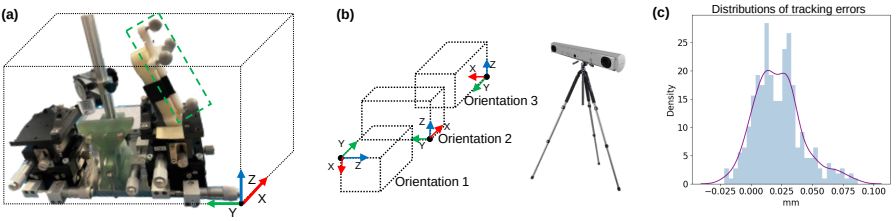

Fig. 4 (a) Optical tracker evaluation setup, 4 optical tracking markers are fixed on a 3-axis micrometer stage. (b) Relative orientations of the micrometer stage w.r.t the optical tracker. (c) Histogram of tracking errors.

the optical tracker (Figure 4 (b)). The histogram of error is plotted in Figure 4 (c). The mean error is 0.02 mm, with a standard deviation of 0.02 mm. The error is small with little variation. Even in the worst-case scenario, the optical tracker has a sub-millimeter error of 0.08 mm.

3.2 Camera Calibration Accuracy

We assess the accuracy of camera calibration as it is critical to downstream applications such as mixed reality. To perform a quantitative evaluation of hand-eye calibration, we record a video sequence of a moving camera observing a static ChArUco pattern. We take the first video frame as the reference frame. The reference frame is transformed and projected into subsequent video frames. We then evaluate the alignment of the projected pattern and observed pattern. We report the re-projection error (RPE) among all frames of size 1080×1920 of a video sequence.

The hand-eye calibration method has a 16 pixels mean RPE. We further convert the RPE to calibration errors by using the projective relationship between pixel and Cartesian coordinate. As the ratio between camera-to-ChArUco distance ${}^{c}t_u$ and focal length f_{px} is equal to the ratio between the calibration error ${}^{c}\epsilon_u$ and mean RPE, we have ${}^{c}t_u/f_{\mathrm{px}} = {}^{c}\epsilon_u/\mathrm{RPE}$. Thus, we can obtain an approximate hand-eye calibration error of 1.9 mm.

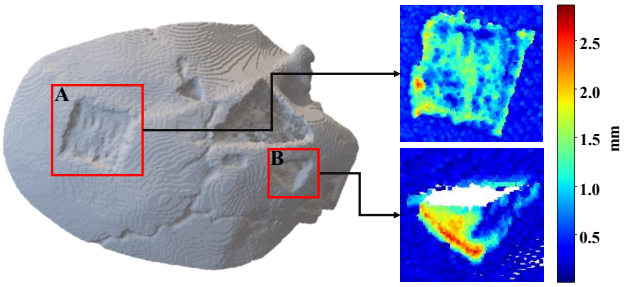

Fig. 5 Evaluation of misalignment between ground truth CT scan and a phantom point cloud from the virtual model. The lower error indicates better agreement between the CT scan and the virtually updated model from Twin-S.

3.3 Drilling Simulation Accuracy

One of the key features of Twin-S is real-time updating of the anatomic model as the model is modified by drilling. Thus, we conduct an experiment to evaluate the accuracy of the simulation during drilling. A surgical expert is invited to drill the surgical phantom similar to *in vivo* surgery, emulating the tissue removal during mastoidectomy.

We compare the updated phantom model of our digital twins after drilling with the 3D structure obtained by a CT scanner (Loop-X, Brainlab). Point clouds are generated from both the virtual phantom model and segmentation of the phantom in the CT scan and aligned using ICP. We visualize the mismatch between the virtual estimate of the tissue ablation and the true state of the phantom after the surgery as a heat map in Figure 5. The mean error of our virtual model in region A is 1.18 mm with a standard deviation of 0.24 mm, and the mean error in region B is 1.61 mm with the standard deviation of 0.49 mm. Errors are mostly located around sharp edges, which are affected to some extent by the limited spatial resolution of the CT scan. Overall, the results indicate that Twin-S can update the anatomical model with a precision comparable to conventional optical navigation systems [22], which is expected since spatial tracking in our digital twins largely relies on those systems.

3.4 Numerically Analyzing Tracking Performance

We quantitatively analyze tracking performance to shed insight into sources of error in the tracking performance. We denote the measured transformation as F^*, which contains error ΔF and deviates from the actual transformation F:

$$F^* = F \cdot \Delta F, \text{ where } \Delta F = \begin{bmatrix} I + \mathrm{sk}(\vec{\alpha}), & \vec{\varepsilon} \\ 0, & 1 \end{bmatrix}. \tag{8}$$

The $I + \mathrm{sk}(\vec{\alpha})$ is the rotational error modeled using axis-angle notation, and $\mathrm{sk}(\cdot)$ is the skew-symmetric matrix. The $\vec{\varepsilon}$ is the translation error.

We present an analysis of the relative pose error between phantom and drill, which is the most critical transformation for modeling tool-to-tissue interactions. The measured phantom to drill transformation is expressed as:

$$\begin{aligned} {}^{d}\mathrm{F}_{p}^{*} &= {}^{o}\mathrm{F}_{d}^{*-1} \cdot {}^{o}\mathrm{F}_{p}^{*}, \\ &= ({}^{o}\mathrm{F}_{db}^{*} \cdot {}^{db}\mathrm{F}_{d}^{*})^{-1} \cdot {}^{o}\mathrm{F}_{pb}^{*} \cdot {}^{pb}\mathrm{F}_{p}^{*}. \end{aligned} \tag{9}$$

In the following content, we use the rotational component as an example to illustrate our derivation and analysis. We expand the error terms of the rotation part and obtain

$$\begin{aligned} {}^{d}R_{p}^{*} &= {}^{db}R_{d}^{*-1} \cdot {}^{o}R_{db}^{*-1} \cdot {}^{o}R_{pb}^{*} \cdot {}^{pb}R_{p}^{*}, \\ {}^{d}R_{p} \cdot \big(I + \mathrm{sk}({}^{d}\vec{\alpha}_{p})\big) &= \Big({}^{db}R_{d} \cdot \big(I + \mathrm{sk}({}^{db}\vec{\alpha}_{d})\big)\Big)^{-1} \cdot \Big({}^{o}R_{db} \cdot \big(I + \mathrm{sk}({}^{o}\vec{\alpha}_{db})\big)\Big)^{-1} \cdot \\ &\quad {}^{o}R_{pb} \cdot \big(I + \mathrm{sk}({}^{o}\vec{\alpha}_{pb})\big) \cdot {}^{pb}R_{p} \cdot \big(I + \mathrm{sk}({}^{pb}\vec{\alpha}_{p})\big). \end{aligned} \tag{10}$$

With re-arrangement, we can obtain 4 independent components contributing to the rotational error:

$${}^{d}\vec{\alpha}_{p} = \beta_{1} \cdot {}^{pb}\vec{\alpha}_{p} + \beta_{2}, \cdot {}^{o}\vec{\alpha}_{pb} + \beta_{3} \cdot {}^{o}\vec{\alpha}_{db} + \beta_{4} \cdot {}^{db}\vec{\alpha}_{d}, \tag{11}$$

$$\text{where } \beta_{1} = I,\ \beta_{2} = {}^{pb}R_{p}^{-1},\ \beta_{3} = -{}^{pb}R_{p}^{-1} \cdot {}^{o}R_{pb}^{-1} \cdot {}^{o}R_{db},\ \beta_{4} = -{}^{d}R_{p}^{-1} \tag{12}$$

Intuitively, the β_i represents how much each measurement error contributes to the final inaccuracy.

To derive the numerical upper bound on tracking error, we use the worst-case tracking accuracy of 0.08 mm for each optical marker obtained from Sect. 3.1. We also assume a worst-case rotation error of 1° for ICP as it is not directly obtainable. We obtain the estimated worst-case error norm as:

$$\begin{aligned} \left\| {}^{d}\vec{\alpha}_{p} \right\|_{2} &\leq \|\beta_{1} \cdot {}^{pb}\vec{\alpha}_{p}\|_{2} + \|\beta_{2}, \cdot {}^{o}\vec{\alpha}_{pb}\|_{2} + \|\beta_{3} \cdot {}^{o}\vec{\alpha}_{db}\|_{2} + \|\beta_{4} \cdot {}^{db}\vec{\alpha}_{d}\|_{2}, \\ &\leq 1.0 + 0.3 + 0.4 + 1.0 = 2.7°. \end{aligned} \tag{13}$$

As shown, the rotational error ${}^{d}\vec{\alpha}_{p}$ is up to 2.7° and dominated by ${}^{pb}\vec{\alpha}_{p}$ and ${}^{db}\vec{\alpha}_{d}$, which are the calibration inaccuracies. A similar analysis can be done on the translation error ${}^{d}\vec{\varepsilon}_{p}$, with the worst error bound of 8.6 mm. Details of the translation error analysis can be found in the appendix.

4 Use Case in Mixed Reality

We explore a mixed reality use case for providing complementary situational awareness using contextually updated virtual content. We consider the scenario where a pre-operative plan is available for the desired bone ablation in the temporal bone. We present a temporally adaptive overlay to encode the

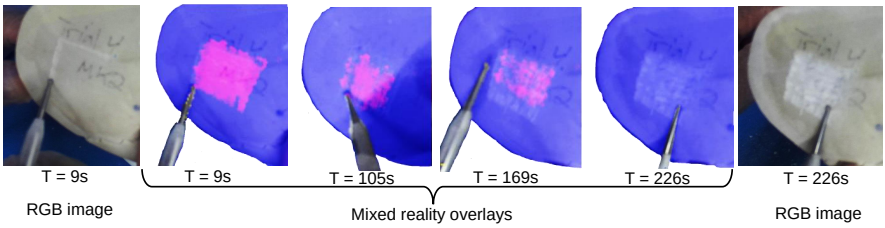

Fig. 6 An illustration of using Twin-S for mixed reality intra-operative guidance. The color overlays generated from the virtual model encode the distance to the deep-seated target.

distance between the current drilled surface and the deeper-seated target. In doing so, we offer depth information that may be difficult for surgeons to observe due to-intervening instruments, bone dust, blood, etc. To demonstrate this idea with Twin-S, we reverse the drilling process and use the final drilled shape as the "pre-planned target" to mimic the targeted application and display the drilling status in previous video frames. Specifically, Twin-S displays a warmer color when the surface is far from the target, and a cooler color as the revealed anatomy is closer to the target. Qualitative visualizations are shown in Figure 6.

We further evaluate the accuracy of virtually generated segmentation masks and report the Dice scores. To obtain ground truth, we manually label a sequence of 100 frames of size 480×640. Using state-of-the-art surgical tool segmentation algorithm[23], the Dice score for the drill is computed as 0.725, and the Dice score for the phantom is 0.956. The lower Dice score of the drill in comparison to the phantom is due to the thin shape of the drill, where slight offsets will lead to much lower Dice scores.

Moreover, we can further generate plothera-paired dataset where images of the surgical scene are paired with virtually generated labels. Through this pairing, we are able to reduce the cost of dataset labeling and avoid the sim-to-real transfer issue commonly faced by synthetic data.

5 Conclusion

We present Twin-S, a digital twin framework for skull-based surgery. Twin-S models, tracks and updates virtual counterparts of physical entities in real-time with high accuracy. We present thorough analysis on the tracking performance and illustrate how Twin-S can be used for downstream applications.

In future work, we plan to integrate vision-based tracking algorithms to further improve the accuracy of Twin-S rather than relying solely on optical trackers. We also plan to conduct *ex vivo* studies to evaluate our system.

Acknowledgments. This work was supported in part by Johns Hopkins University internal funds and in part by NIDCD K08 Grant DC019708.

References

[1] Inc., I.: What is a digital twin? | IBM. https://www.ibm.com/topics/what-is-a-digital-twin Accessed 2022-8-13

[2] Jones, D., Snider, C., Nassehi, A., Yon, J., Hicks, B.: Characterising the Digital Twin: A systematic literature review. CIRP Journal of Manufacturing Science and Technology (2020)

[3] Coelho, G., Rabelo, N.N., Vieira, E., Mendes, K., Zagatto, G., Santos de Oliveira, R., Raposo-Amaral, C.E., Yoshida, M., de Souza, M.R., Fagundes, C.F., Teixeira, M.J., Figueiredo, E.G.: Augmented reality and physical hybrid model simulation for preoperative planning of metopic craniosynostosis surgery. Neurosurgical Focus (2020)

[4] Chalasani, P., Wang, L., Roy, R., Simaan, N., Taylor, R.H., Kobilarov, M.: Concurrent nonparametric estimation of organ geometry and tissue stiffness using continuous adaptive palpation. In: Proc. ICRA (2016)

[5] Wang, L., Chen, Z., Chalasani, P., Yasin, R.M., Kazanzides, P., Taylor, R.H., Simaan, N.: Force-controlled exploration for updating virtual fixture geometry in model-mediated telemanipulation. Journal of Mechanisms and Robotics (2017)

[6] Yasin, R., Chalasani, P., Zevallos, N., Shahbazi, M., Li, Z., Deguet, A., Kazanzides, P., Choset, H., Taylor, R.H., Simaan, N.: Evaluation of hybrid control and palpation assistance for situational awareness in telemanipulated task execution. IEEE TMRB (2020)

[7] Lungu, A.J., Swinkels, W., Claesen, L., Tu, P., Egger, J., Chen, X.: A review on the applications of virtual reality, augmented reality and mixed reality in surgical simulation: an extension to different kinds of surgery. Expert Review of Medical Devices (2021)

[8] Aguilar-Salinas, P., Gutierrez-Aguirre, S.F., Avila, M.J., Nakaji, P.: Current status of augmented reality in cerebrovascular surgery: a systematic review. Neurosurgical Review (2022)

[9] Kockro, R.A., Tsai, Y.T., Ng, I., Hwang, P., Zhu, C., Agusanto, K., Hong, L.X., Serra, L.: Dex-ray: augmented reality neurosurgical navigation with a handheld video probe. Neurosurgery (2009)

[10] Agha, R.A., Fowler, A.J.: The Role and Validity of Surgical Simulation. International Surgery (2015)

[11] Munawar, A., Li, Z., Kunjam, P., Nagururu, N., Ding, A.S., Kazanzides, P., Looi, T., Creighton, F.X., Taylor, R.H., Unberath, M.: Virtual Reality

for Synergistic Surgical Training and Data Generation. Comp. Meth. in Biomech. and Biomed. Eng.: Imaging & Visualization (2021)

[12] Shi, Y., Deng, X., Tong, Y., Li, R., Zhang, Y., Ren, L., Si, W.: Synergistic Digital Twin and Holographic Augmented-Reality-Guided Percutaneous Puncture of Respiratory Liver Tumor. IEEE Trans. HMS (2022)

[13] Laaki, H., Miche, Y., Tammi, K.: Prototyping a Digital Twin for Real Time Remote Control Over Mobile Networks: Application of Remote Surgery. IEEE Access (2019)

[14] Bonne, S., Panitch, W., Dharmarajan, K., Srinivas, K., Kincade, J.-L., Low, T., Knoth, B., Cowan, C., Fer, D., Thananjeyan, B., Kerr, J., Ichnowski, J., Goldberg, K.: A Digital Twin Framework for Telesurgery in the Presence of Varying Network Quality of Service. In: Proc. CASE (2022)

[15] Razavi, C.R., Wilkening, P.R., Yin, R., Barber, S.R., Taylor, R.H., Carey, J.P., Creighton, F.X.: Image-Guided Mastoidectomy with a Cooperatively Controlled ENT Microsurgery Robot. OtolaryngologyHead and Neck Surgery (2019)

[16] Yaniv, Z.: Which pivot calibration? In: Medical Imaging 2015: Image-guided Procedures, Robotic Interventions, and Modeling (2015). SPIE

[17] Kabsch, W.: A solution for the best rotation to relate two sets of vectors. Acta Crystallographica Section A (1976)

[18] Chen, Y., Medioni, G.: Object modelling by registration of multiple range images. Image and Vision Computing (1992)

[19] Zhang, Z.: A flexible new technique for camera calibration. IEEE Transactions on pattern analysis and machine intelligence (2000)

[20] Horaud, R., Dornaika, F.: Hand-eye calibration. The International Journal of Robotics Research (1995)

[21] Furrer, F., Fehr, M., Novkovic, T., Sommer, H., Gilitschenski, I., Siegwart, R.: Evaluation of Combined Time-Offset Estimation and Hand-Eye Calibration on Robotic Datasets. In: Field and Service Robotics, (2018)

[22] Holland, M.T., Mansfield, K., Mitchell, A., Burchiel, K.J.: Hidden error in optical stereotactic navigation systems and strategy to maximize accuracy. Stereotactic and Functional Neurosurgery (2021)

[23] Ding, H., Zhang, J., Kazanzides, P., Wu, J.Y., Unberath, M.: Carts: Causality-driven robot tool segmentation from vision and kinematics data. In: Proc. MICCAI (2022)